

CHAPTER 6

Electron–Nuclear Double Resonance

C.A.J. AMMERLAAN

*Natuurkundig Laboratorium
University of Amsterdam
The Netherlands*

and

J.R. NIKLAS

*Fachbereich 6, Experimentalphysik
University of Paderborn
Germany*

© Elsevier Science Publishers B.V., 1992

*Hyperfine Interaction of
Defects in Semiconductors
Edited by G. Langouche*

Contents

1. Introduction	259
1.1. Principles	259
1.2. Transient ENDOR	259
1.3. Stationary ENDOR	260
1.4. Sensitivity	261
1.5. Resolution	262
2. ENDOR-induced EPR	262
2.1. Principles	262
2.2. Nuclear spin $I > \frac{1}{2}$	265
3. Double ENDOR	267
4. Impurity ENDOR	270
4.1. Spin Hamiltonian	270
4.2. Nuclear Zeeman effect BI	271
4.3. Hyperfine interaction SI	275
4.4. Electron–nuclear interaction S^3I	276
4.5. Electron–nuclear interaction S^2I^2	277
5. Ligand–atom ENDOR	278
5.1. Ligand–atom shells	278
5.2. LCAO analysis	278
5.3. Minimum-transferred spin density	282
References	284

1. Introduction

1.1. Principles

Electron–nuclear double resonance (ENDOR) is the simultaneous application of electron paramagnetic resonance (EPR) and nuclear magnetic resonance (NMR). Obviously, the feasibility of the method requires a physical system with paramagnetic centres, electron spin $S \neq 0$, and with nuclear magnetic momenta spin(s) $I \neq 0$. In ENDOR both resonances are applied under such conditions that an interference between the two resonances occurs. Then the induction of one of the resonances has an influence on the other resonance. Pioneering studies developing the principles of ENDOR were carried out by Feher and Gere (Feher 1956a, b, Feher and Gere 1956). First demonstrations of its power in the spectroscopic research of solids concerned phosphorus and other donors in silicon (Feher et al. 1957, Feher 1959) and the F centre in KCl (Feher 1957). The method allows to benefit from the advantageous features of each of the resonances. The advantages that make ENDOR extremely beneficial as a spectroscopic tool is that it can combine the high energy resolution of NMR with the high sensitivity of EPR. To observe ENDOR, the EPR and NMR resonance conditions have to be satisfied simultaneously. Usually, this is achieved by first optimizing the EPR signal, by scanning the magnetic field at constant microwave frequency. Subsequently, at constant magnetic field, the radio-frequency is scanned to satisfy the NMR condition. An alternative scheme, revealing the EPR underlying an observed ENDOR signal, called ENDOR-induced EPR, is discussed in section 2. Also, the method may be extended to multiple resonance. An example of triple resonance involving one electron and two nuclei is discussed in section 3. ENDOR allows detailed studies of the atomic and electronic structures of paramagnetic centres in semiconductors to be made. A discussion on the analysis and further physical interpretation of spectroscopic data is given for the system of interstitial titanium in silicon in sections 4 and 5.

1.2. Transient ENDOR

For the application of transient ENDOR the values of magnetic field and microwave frequency are adjusted to obey the electron resonance condition. This is indicated for transition $h\nu_{e1}$ in fig. 1b within the four energy levels of the simplest spin system with $S = \frac{1}{2}$ and $I = \frac{1}{2}$. The microwave power is chosen high enough to saturate the transition. The populations of the two levels linked by the transition become equal and the EPR signal will be small.

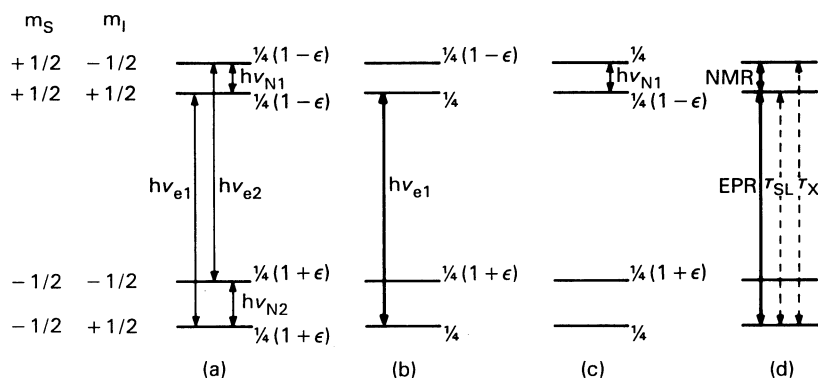


Fig. 1. Energy levels of the spin system $S = \frac{1}{2}$, $I = \frac{1}{2}$ in an externally applied large magnetic field, and normalized level populations under various conditions: (a) populations in thermal equilibrium, nuclear Boltzmann factor ignored; (b) with saturation of the EPR transition $h\nu_{e1}$; (c) after adiabatic fast passage through the NMR transition $h\nu_{N1}$; (d) labelling by dashed lines of the spin-lattice relaxation path τ_{SL} and the cross-relaxation path τ_X .

Under these conditions, an NMR transition is induced; for instance, the transition connecting the highest two states in fig. 1. The NMR transition will lower the population of the $|+\frac{1}{2}, +\frac{1}{2}\rangle$ level, resulting in a transient increase of the EPR amplitude. This is the characteristic feature of the ENDOR method: the induction of nuclear magnetic resonance is observed by a change of the electron spin resonance intensity. The induction of the nuclear magnetic resonance may either be a saturation at high radio-frequency power, equalizing the level populations, or an adiabatic fast passage, in which the populations of the levels are reversed. The latter case is illustrated in fig. 1c. ENDOR based on this mechanism produces only a transient signal. Feher's first ENDOR experiments are examples of the transient ENDOR technique. One of his results for arsenic donors in silicon (Feher 1959) is shown in fig. 2a.

1.3. Stationary ENDOR

As in the previous case, one of the EPR transitions is saturated. The amplitude of the EPR line will depend on the spin-lattice relaxation time τ_{SL} . The relaxation path between the two levels is indicated by τ_{SL} in fig. 1d. If now the upper two nuclear sublevels are short-circuited by the application of a radio-frequency at saturation power, a second relaxation path via cross-relaxation becomes effective. The two mechanisms acting in parallel will result in a slightly smaller effective relaxation time, $\tau = \tau_{SL}\tau_X/(\tau_{SL} + \tau_X)$. As the EPR amplitude depends on the actual relaxation rate, the change in τ will

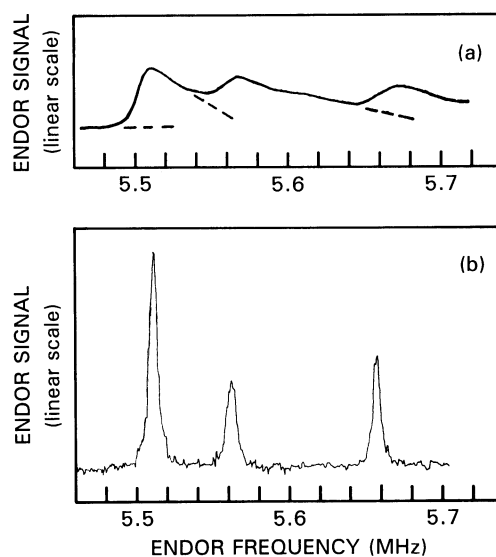


Fig. 2. ENDOR spectra observed in arsenic-doped silicon: (a) transient ENDOR after Feher (1959); (b) stationary ENDOR after Hale and Miehler (1969).

result in a steady change of EPR amplitude. This represents the stationary ENDOR signal. Shallow donors in silicon were investigated in detail by Hale and Miehler (1969) under conditions of stationary ENDOR. Their result for arsenic in silicon is reproduced in fig. 2b.

1.4. Sensitivity

The net number of transitions, i.e. absorptions minus emissions, induced when applying radiation of the resonant frequency is proportional to the difference in the population of the two levels involved. In thermal equilibrium, as in fig. 1a, this is governed by the Boltzmann factors of the levels as split by the electronic and nuclear Zeeman energies. Under the usual conditions of the resonance experiment, the population difference between nuclear levels is typically 1000 times smaller than that between levels of different electronic spin. In the ENDOR method the population of two levels is substantially changed by saturation through high microwave power. Two adjacent levels connected by the radio-frequency inducing the nuclear transitions can now have a population difference that is characterised by the larger electronic Boltzmann factor. This represents a considerable enhancement of the sensitivity over the direct method. The level populations

become, moreover, independent of the nuclear magnetic moment. This implies that nuclei with small moments do not suffer the usual loss of sensitivity.

1.5. Resolution

In section 2 the model system of one electron, $S = \frac{1}{2}$, interacting with N surrounding nuclei, each with $I = \frac{1}{2}$, is considered. In EPR the resonance field as given by eq. (2) is influenced by the nuclear quantum numbers of all the nuclei, of which there are 2^N different combinations. In many cases the separation between the many possible resonance fields is less than the homogeneous linewidth of the individual spin packets. In such a case the EPR line cannot be resolved into its constituting components. The line is inhomogeneously broadened. Only its envelope can be measured. The NMR frequency of each nucleus, $k = 1, \dots, N$, is given by eq. (6), with $m_S = \pm \frac{1}{2}$. The number of lines in the spectrum is $2N$. Each of these has its natural homogeneous linewidth, to which a possible unresolved inhomogeneous broadening due to interactions between the nuclei has to be added. In many practical cases the NMR linewidth is 3 to 4 orders of magnitude smaller than that for EPR. This represents an enormous gain in the resolving power. The basic difference is that in EPR one observes the resonance of the defect electron which experiences the interactions with all the nuclei at the same time. In the NMR and ENDOR, on the other hand, one resonates one nucleus at a time, which feels only one electron interaction, and the other nuclei only feebly.

2. ENDOR-induced EPR

2.1. Principles

When considering the ENDOR mechanism, there is an important point which needs further consideration. Apparently, the NMR transition to be detected via EPR must involve exactly the same level which is involved also in the EPR transition. Otherwise, it is not clear in which way a desaturation of the EPR transition could take place with optimum efficiency. The question that arises now is: In which way in an ENDOR experiment can the microwave frequency and the magnetic field be adjusted so precisely that the EPR transition exactly hits the levels involved in the NMR transitions. In order to clarify the question in a more systematic way, it is useful to consider once again the EPR transitions, but in quite an unusual way. For the following arguments, a model system where an electron spin interacts with N neighbour nuclei ($N \geq 2$) is considered. All neighbour nuclei are assumed to have

nuclear spin $I = \frac{1}{2}$. The possible EPR transition energies $h\nu$ are then simply given by

$$h\nu = g_e\mu_B B + \sum_{i=1}^N A_i m_{I_i}. \quad (1)$$

Since in an EPR experiment the microwave frequency is kept constant and the magnetic field is varied, eq. (1) may be expressed in the form

$$B = h\nu/(g_e\mu_B) - \sum_{i=1}^N A_i m_{I_i}/(g_e\mu_B). \quad (2)$$

All possible EPR lines within the entire spectrum can now be considered as being due to all possible combinations of values for the m_{I_i} under the summation sign. Since all neighbour nuclei exhibit nuclear spin $I = \frac{1}{2}$, each m_{I_i} can be either $+\frac{1}{2}$ or $-\frac{1}{2}$. There are 2^N possibilities to assign these two values to the different m_{I_i} . The EPR spectrum according to eq. (2) consists, therefore, of 2^N lines. Since each of these lines has a very small, but finite, natural linewidth, the density of these lines around a magnetic field within the field range of the natural linewidth is observed as the intensity of the EPR spectrum at this field. Equation (2) may now be expressed in a slightly different way, with no effect on its physical meaning:

$$B = h\nu/(g_e\mu_B) - \sum_{i=1, i \neq k}^N (A_i m_{I_i}/(g_e\mu_B)) - A_k m_{I_k}/(g_e\mu_B), \quad (3)$$

where k is some number between 1 and N . The term with the number k is no longer part of the sum, it is subtracted separately. The spin quantum number m_{I_k} of the neighbour k again has two possible values $m_{I_k} = \pm \frac{1}{2}$. Even if by a suitable radio-frequency field, transitions are induced between these two levels during the measurement of the conventional EPR, this has no noticeable effect on the EPR spectrum. All possible spin states as discussed in eq. (2) are still present with the same probability as considered above.

We now use the neighbour nucleus k for an ENDOR experiment. There are four possible levels for the interaction of the electron spin with this neighbour nucleus k . These levels correspond to $m_S = \pm \frac{1}{2}$ and $m_{I_k} = \pm \frac{1}{2}$, respectively. At the magnetic field B_0 their energies E are given by

$$E = g_e\mu_B B_0 m_S + A_k m_{I_k} m_S - g_N \mu_N B_0 m_{I_k}. \quad (4)$$

There are two possible EPR transition energies:

$$h\nu_{\text{EPR}} = g_e\mu_B B_0 + A_k m_{I_k}, \quad (5)$$

where $m_{I_k} = \pm \frac{1}{2}$, and there are two possible NMR transition energies for the

ENDOR process:

$$\hbar\nu_{\text{NMR}} = |A_k m_S - g_{\text{N}k} \mu_{\text{N}} B_0|, \quad (6)$$

where $m_S = \pm \frac{1}{2}$. The question now is, whether an ENDOR signal of the same neighbour nucleus k can also be observed with the same EPR transition energy (fixed microwave frequency of the spectrometer) but at a different magnetic field, B'_0 , within the EPR spectrum. The answer is straightforward. Since B'_0 is within the EPR spectrum, it must satisfy eq. (3). Consequently, there must exist sets of nuclear quantum numbers m_{Ii} , $i \neq k$, such that

$$B'_0 = h\nu_{\text{EPR}}/(g_e \mu_{\text{B}}) - \sum_{i=1, i \neq k}^N (A_i m_{Ii}/(g_e \mu_{\text{B}})) - A_k m_{Ik}/(g_e \mu_{\text{B}}). \quad (7)$$

Comparison of this equation with eq. (5) immediately yields

$$B_0 = B'_0 + \sum_{i=1, i \neq k}^N A_i m_{Ii}/(g_e \mu_{\text{B}}). \quad (8)$$

This means that if one uses a different magnetic field within the EPR spectrum, then all the other nuclei with number i , $i \neq k$, are able to add an extra field in a way that the ENDOR process for the neighbour k according to eq. (4) is again possible. Consequently, an ENDOR signal of the neighbour k can be measured at any magnetic field within the EPR spectrum. The shape of the EPR spectrum makes no difference. However, due to the nuclear Zeeman term in eq. (6) the ENDOR frequency is shifted by an amount

$$|\Delta\nu_{\text{NMR}}| = |g_{\text{N}k} \mu_{\text{N}} (B'_0 - B_0)|/h. \quad (9)$$

This shift can be used to measure the nuclear g value g_{Ik} and, thus, to determine the chemical identity of the neighbour k . (For many practical cases this first-order expression is, however, not sufficiently accurate.)

Scanning the frequency of the radio-frequency (RF) field results in selecting different neighbours k for the ENDOR measurement. Since k may have any value between 1 and N , the above arguments are valid for the entire ENDOR spectrum containing signals of all neighbour nuclei. One obtains, therefore, ENDOR spectra with identical information for any value of B_0 within the EPR spectrum. However, there is still an important difference between the ENDOR spectra measured at different magnetic fields. As mentioned above, the signal intensity of the EPR spectrum for a given value of B_0 depends on the number of values, according to eq. (2), which fall into the small interval $[B_0, B_0 \pm \Delta B_0]$, where $\Delta B_0/B_0$ is of the order of 10^{-5} . Or, in other words, the EPR intensity at the field B_0 is proportional to the probability that a calculated field value, according to eq. (2), for all possible combinations of m_{Ii} falls into the interval $[B_0, B_0 \pm \Delta B_0]$. The same arguments hold for the magnitude of the ENDOR process as a function of the magnetic field. The

magnitude of the ENDOR signal observed for the neighbour k at the magnetic field B'_0 is proportional to the probability that the neighbour nuclei, according to eq. (8), add the extra field necessary to enable the ENDOR process according to eqs. (4)–(6). The same term which produces the extra field in eq. (8) determines the EPR signal intensity at the field B'_0 , according to eq. (7). Therefore, the ENDOR signal intensity is proportional to the EPR intensity at the magnetic field used for the ENDOR measurement. If one scans the magnetic field over the entire range of the EPR spectrum during an ENDOR measurement, the amplitude of each ENDOR line will reproduce the shape of the EPR spectrum. The ENDOR lines are slightly shifted as a function of the magnetic field [see eq. (9)], which has nothing to do with their amplitude. When performing such a field scan experiment, the ENDOR frequency must be adjusted accordingly [see eq. (9)]. This kind of experiment is called 'ENDOR-induced EPR' (EI-EPR).

So far only the simplified case was considered, where all neighbour nuclei have $I = \frac{1}{2}$. It can, however, easily be seen from the arguments given above that it is still possible to reproduce the EPR spectrum via an ENDOR signal also for arbitrary nuclear neighbour spins. The only condition is that the ENDOR signal used to reproduce the EPR spectrum comes from a nucleus with $I = \frac{1}{2}$ (100% abundant). Otherwise, the EPR spectrum reproduced is different from the original EPR spectrum.

The possibility to measure ENDOR-induced EPR spectra provides a very useful experimental tool. It enables one to separate overlapping EPR spectra due to different defects present simultaneously and to separate the parts of the EPR spectrum of a low-symmetry defect, which correspond to different defect orientations. If in an ENDOR spectrum lines are present from different defects, then each ENDOR line can be assigned to its defect by measuring the corresponding EPR spectrum via the ENDOR line. Applications are summarized in Niklas and Spaeth (1980) and Spaeth and Niklas (1981). As an example, fig. 3b shows the superimposed EPR absorption spectra of S^+ (isotropic, $g_e = 2.0054$) and $(S-S)^+$ pairs (isotropic, $g_e = 2.0008$) in silicon (Greulich-Weber 1987). These spectra are separated by ENDOR-induced EPR (fig. 3c and d) using the ENDOR lines ν_2 and ν_1 , respectively.

2.2. Nuclear spin $I > \frac{1}{2}$

The situation is slightly more complicated if, for the measurement of EI-EPR, an ENDOR line of a nucleus with $I > \frac{1}{2}$ is used. In this case the separate term with the number k [see eq. (3)] contributes more than one EPR transition to the EPR spectrum. Any NMR transition at the nucleus k is, however, no longer able to affect all possible EPR transitions for this nucleus at a time in first order. As a consequence, the ENDOR-induced EPR

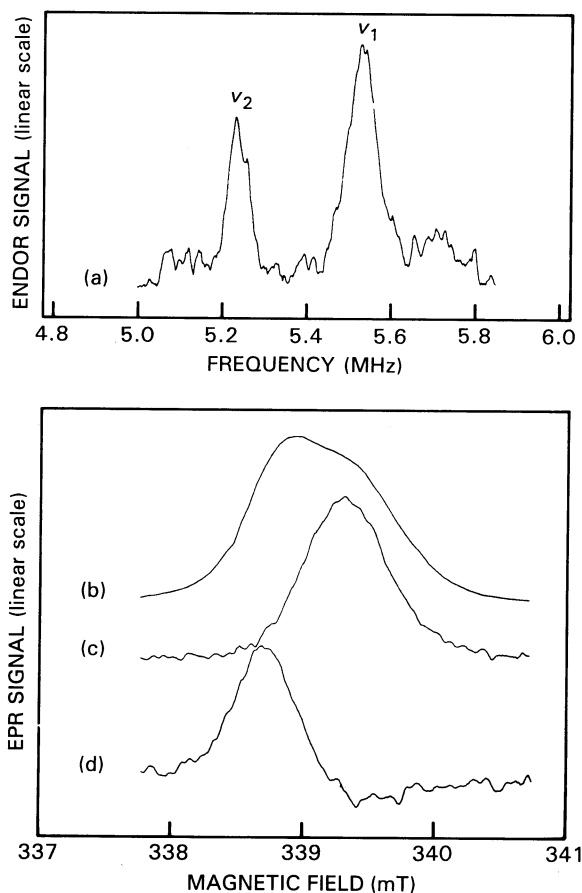


Fig. 3. ENDOR-induced EPR for S^+ and $(S-S)^+$ pairs in silicon: (a) part of the ENDOR spectrum containing lines of both centres; (b) superimposed EPR absorption spectra of both centres; (c) ENDOR-induced EPR spectrum for the ENDOR line ν_2 of the centre $(S-S)^+$; (d) ENDOR-induced EPR spectrum for the ENDOR line ν_1 of the centre S^+ (Greulich-Weber 1987).

spectrum may be shifted compared to the original EPR spectrum or may exhibit a smaller half-width, depending upon the ENDOR line chosen for the experiment. This effect can be used to determine relative signs of superhyperfine and quadrupole interaction constants (Niklas and Spaeth 1980).

For $S > \frac{1}{2}$ the mechanism of EI-EPR works as well. Again only a subset of all possible m_s values is contained in the EI-EPR spectrum. When taking different NMR transitions coupled to different m_s states, one can measure different subspectra of the original EPR spectrum, which correspond to

different values of m_S . This enables one to determine relative signs of fine structure, hyperfine, or superhyperfine interaction constants (DuVarney et al. 1981). With EI-EPR it is also possible to investigate a fine-structure splitting which is not resolved in the EPR spectrum, as applied e.g. to Ni^{3+} defects in GaP (Ueda et al. 1983). For further details see Niklas and Spaeth (1980).

3. Double ENDOR

ENDOR-induced EPR provides a useful tool to assign ENDOR lines to their corresponding EPR spectra in the case of overlapping EPR spectra. However, since all of the many ENDOR lines from these different defects are present, the large number of lines can make analysis of the spectra very difficult. ENDOR-induced EPR is useful only as long as the separated EPR spectra are sufficiently different from each other. This is often not the case. It is, therefore, desirable to have some measurement technique which delivers the individual ENDOR spectra for each defect separately right from the beginning. Such an experiment is indeed possible.

The effectiveness of an ENDOR process depends strongly on the type of relaxation by-passes provided by many other neighbour nuclei not directly involved in the ENDOR process. Such a relaxation by-pass, which affects the magnitude of an ENDOR signal, can also be provided by an additional NMR transition, which is simultaneously induced by a second radio-frequency. A simple model system to illustrate this is shown in fig. 4 for the interaction of an electron with two neighbour nuclei with $I_1 = I_2 = \frac{1}{2}$. It is quite obvious from the figure that the induced NMR transition between the levels 7 and 8, W_{n2} , has less effect on the desaturation of the EPR transition between the levels 1 and 8, W_e , if an additional RF transition, W_{n1} , is induced between the levels 6 and 8. In this case the relaxation by-pass through the levels 8, 6, 3 and 1 becomes more efficient, diminishing the ENDOR process involving the levels 1, 8 and 7. The same result is present, in principle, if there are more than two neighbour nuclei present and if the nuclear spin of these nuclei exceeds $\frac{1}{2}$. This can be easily verified by rate equation calculations (Niklas et al. 1983). An ENDOR process is always diminished if the two NMR transitions take place at nuclear levels belonging to the same m_S . It can also be seen from fig. 4 that an ENDOR effect is enhanced if the two NMR transitions take place at different m_S levels. This is particularly obvious if one NMR transition takes place between the levels 7 and 8 for $m_S = +\frac{1}{2}$ and the levels 1 and 2 for $m_S = -\frac{1}{2}$. In this special case the two transitions take place at the same nucleus, but at different radio-frequencies for different m_S levels. This case is called 'special triple resonance' (Biehl et al. 1975). Also, in the

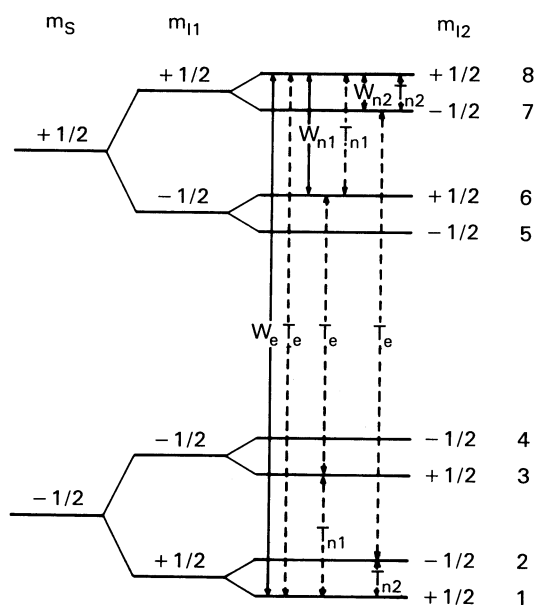


Fig. 4. Energy level scheme for the interaction of an electron spin $S = \frac{1}{2}$ with two neighbour nuclei with $I_1 = I_2 = \frac{1}{2}$ to explain triple resonance processes. For details see the text.

general case, where the two NMR transitions take place at different neighbour nuclei for different m_S values, always an enhancement of an ENDOR effect occurs.

In a special measurement technique, the effects described above can be used to separate ENDOR spectra due to different defects. It turns out, experimentally, that an ENDOR signal is changed by not more than about 10% when a second NMR transition is induced. It is, therefore, necessary to detect the change of the ENDOR signal upon switching on and off the second radio-frequency, with high sensitivity using lock-in techniques. Usually, an ENDOR signal is detected by modulating the RF source and observing the corresponding change of the EPR signal using lock-in techniques. In the case of triple resonance, one modulates the second radio-frequency with a second frequency considerably lower than the first modulation frequency and observes the triple resonance signal with a second lock-in amplifier connected in series to the first one. In this measurement configuration no signal is observed if the two RF transitions take place at the two nuclei which belong to different defects. No signal is observed because there is no mutual influence of the two NMR transitions in this case. The detection technique is insensitive to additive effects of the two NMR transitions. Thus, it is possible to sensitise with the first radio-frequency one centre, by adjusting the frequency to one of

its ENDOR lines, for the exclusive measurement of its ENDOR spectrum by the second radio-frequency.

Another important application of double ENDOR is the distinction between low- and high-symmetry defects. An experimental example is shown in fig. 5. The dots show a part of the first 111-neighbour shell of P neighbours of the paramagnetic Ga vacancy in GaP ($S = \frac{3}{2}$) (Hage et al. 1986). There are two ENDOR lines instead of one for $m_S = +\frac{3}{2}$ and $m_S = -\frac{3}{2}$, respectively. (See arrow at 70° in fig. 5.) Each of the two lines expected from symmetry is split by about 5 MHz due to indirect coupling between the first four P neighbours. Their superhyperfine interaction energy W_{shf} of about 200 MHz, in frequency units, is sufficiently large compared to the electron Zeeman energy of about 10 GHz to give rise to this effect. For the determination of the defect model these lines splittings can be very helpful because one can determine the number of nuclei in the neighbour shell by an analysis of such splittings. On the other hand, it may be sometimes difficult to tell whether an observed line splitting is due to this effect or due to a lower symmetry of the defect than expected, or both. In this case double-ENDOR experiments can give a definite answer. For the Ga vacancy in GaP (fig. 5) this is demonstrated in fig. 6. Figure 6a shows the ENDOR spectrum for $B_0 \parallel [111]$, as indicated by the arrow at about 35° in fig. 5. Figure 6b shows the corresponding double-ENDOR spectrum, where the first radio-frequency was adjusted to

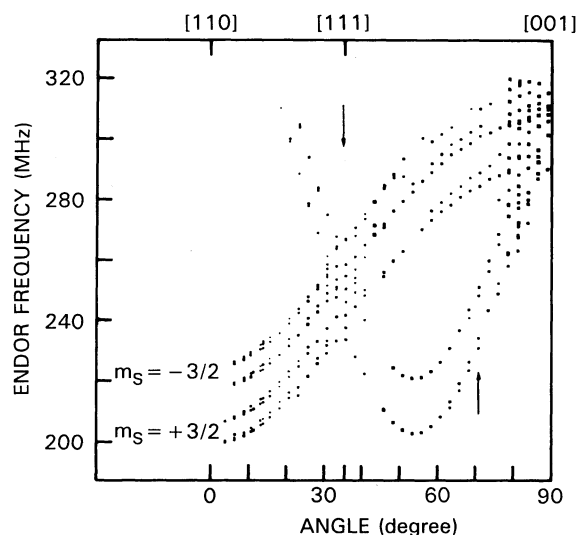


Fig. 5. Experimental ENDOR angular dependence of the first P 111-neighbour shell of the paramagnetic Ga vacancy in GaP with a second-order hyperfine structure. The magnetic field was varied in a (110) plane starting along $B_0 \parallel [110]$ (0°) and ending along $B_0 \parallel [001]$ (90°) (Hage et al. 1986).

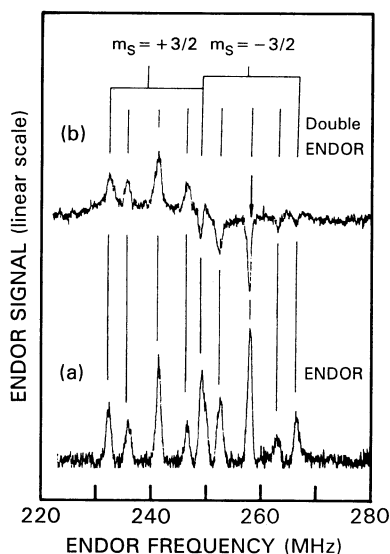


Fig. 6. (a) ENDOR spectrum extracted out of the angular dependence in fig. 5 for $B_0 \parallel [111]$ (indicated by the arrow at about 35° in fig. 5); (b) the corresponding double-ENDOR spectrum with the first frequency adjusted to the most prominent line of the spectrum in fig. 6a (Hage et al. 1986).

the most prominent line in the ENDOR spectrum (arrow in fig. 6). Each ENDOR line is reflected by a corresponding double-ENDOR line demonstrating that all lines definitely belong to the same defect. It can, therefore, be excluded that some of the lines could belong to different orientations of a low-symmetry defect. The defect must, therefore, have the same high symmetry as the host crystal, and the observed lines are, in this case, indeed due to pseudo-dipolar couplings.

4. Impurity ENDOR

4.1. Spin Hamiltonian

Impurity ENDOR, or self-ENDOR, measures the interaction between the defect electron and the nucleus (or nuclei) in the core of a paramagnetic centre. These interactions are expressed and conveniently analysed using an appropriate spin Hamiltonian. The number and character of the terms required depends on the symmetry of the centre and the values of the electronic and nuclear spins. An illustrative example is provided by the system of the transition element titanium in silicon (Van Wezep and

Ammerlaan 1985, 1988). The impurity occupies an interstitial lattice site with $\bar{4}3m$ ($\equiv T_d$) symmetry. In the observed positive-charge state the electronic configuration is $3d^3$. According to Hund's rule, the spins are parallel in the ground state, which results in an electronic spin of $S = \frac{3}{2}$. In the ENDOR experiments samples were used doped with titanium highly enriched in one of its magnetic isotopes. Both the isotopes ^{47}Ti , with nuclear spin $I = \frac{5}{2}$, and ^{49}Ti , with $I = \frac{7}{2}$, were investigated. Due to the high values of spins, higher-order terms may appear in the spin Hamiltonian. For the present case, with cubic symmetry, the expression required for satisfactory analysis is

$$\begin{aligned}
\mathcal{H} = & + g_e \mu_B (B_x S_x + B_y S_y + B_z S_z) \\
& - g_N \mu_N (B_x I_x + B_y I_y + B_z I_z) \\
& + A (S_x I_x + S_y I_y + S_z I_z) \\
& + U \{ S_x^3 I_x + S_y^3 I_y + S_z^3 I_z \\
& - \frac{1}{5} [3S(S+1) - 1] (S_x I_x + S_y I_y + S_z I_z) \} \\
& + a [(S_x S_y + S_y S_x) (I_x I_y + I_y I_x) + (S_y S_z + S_z S_y) (I_y I_z + I_z I_y) \\
& \quad + (S_z S_x + S_x S_z) (I_z I_x + I_x I_z)] \\
& + b \{ + [3S_x^2 - S(S+1)] [3I_x^2 - I(I+1)] \\
& \quad + [3S_y^2 - S(S+1)] [3I_y^2 - I(I+1)] \\
& \quad + [3S_z^2 - S(S+1)] [3I_z^2 - I(I+1)] \}. \tag{10}
\end{aligned}$$

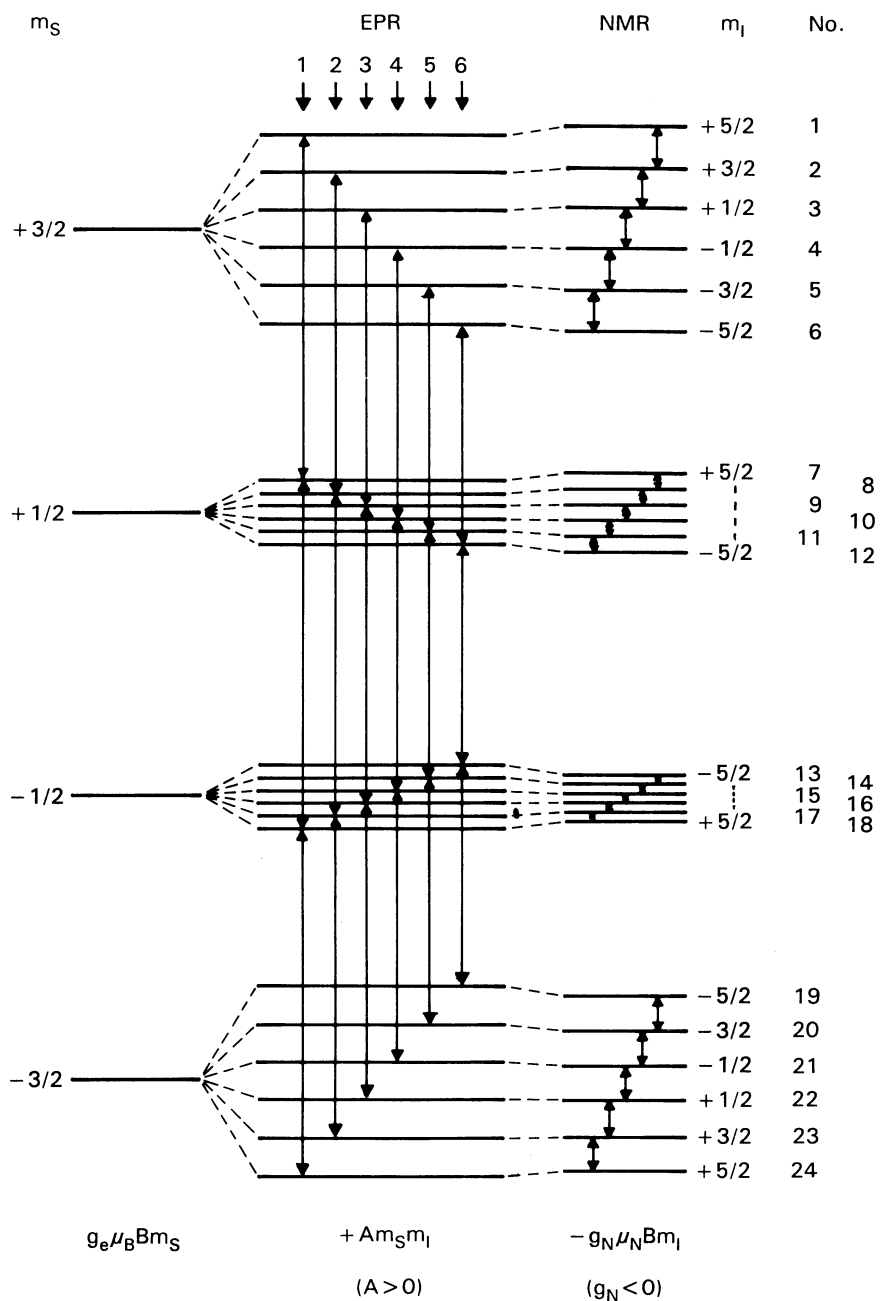
The first three terms, representing the usual electron and nuclear Zeeman and the hyperfine interaction, give the level diagram with EPR and NMR transitions, as illustrated in fig. 7. For these interactions, all with scalar coupling constants, isotropic ENDOR frequencies are expected. In the experiment, however, an angle-dependent variation was observed. Rotating the magnetic field in the $(0\bar{1}1)$ plane by an angle θ with the $[100]$ direction, the angular variation was found to be proportional to

$$p(\theta) = 1 - 5 \sin^2 \theta + \frac{15}{4} \sin^4 \theta. \tag{11}$$

The illustration for some transitions is given in fig. 8. Such a variation is indicative of interactions which are fourth-order in the spins. Interactions of the type $S^3 I$ and $S^2 I^2$ are, therefore, included in the Hamiltonian.

4.2. Nuclear Zeeman effect BI

The free nucleus has a gyromagnetic ratio γ and g value g_N which can be found in tables (Fuller 1976). The free electron has g value $g_{fe} = 2.0023$. For a



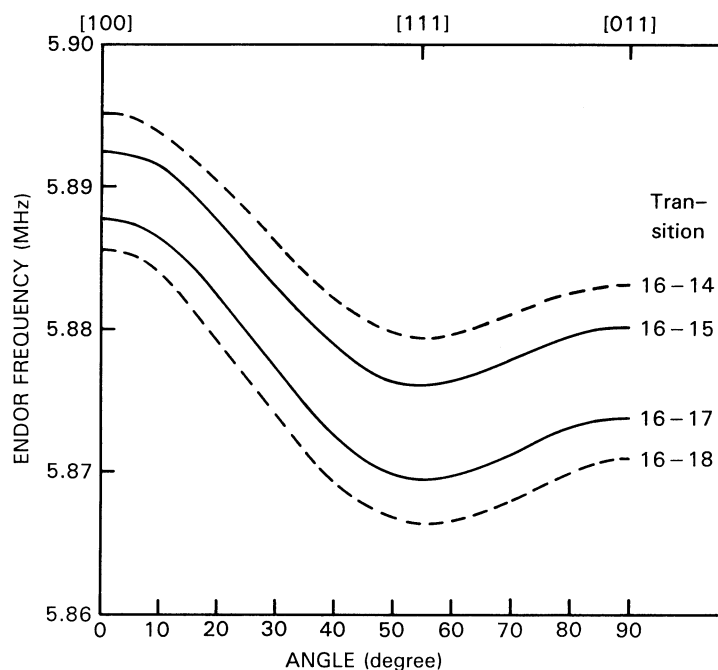


Fig. 8. Angular dependence of ENDOR frequencies for Si: $^{47}\text{Ti}^+$, rotation of magnetic field B in the $(0\bar{1}1)$ plane. Single quantum transitions (solid lines) and double quantum transitions (dashed lines) involving level 16 are shown. For labelling of levels, see fig. 7.

centre in a solid both g values are altered by effects of shielding, covalency, or presence of orbital angular momentum. The system Si: Ti^+ has an orbital singlet $^4\text{A}_2$ ground state. However, due to spin–orbit interaction higher states are mixed into the ground state. Figure 9 gives the simplest level structure with excited states $^4\text{T}_1$ and $^4\text{T}_2$. In this model a second-order perturbation treatment, as presented by Low (1960), gives for the adjusted g values

$$(g_e)_{ij} = g_{fe}(\delta_{ij} - \lambda A_{ij}), \quad (12)$$

$$(g_N)_{ij} = g_N \delta_{ij} + 2P\mu_B A_{ij}/\mu_N, \quad (13)$$

Fig. 7. Energy levels of the spin system $S = \frac{3}{2}$, $I = \frac{5}{2}$ in an externally applied magnetic field B .

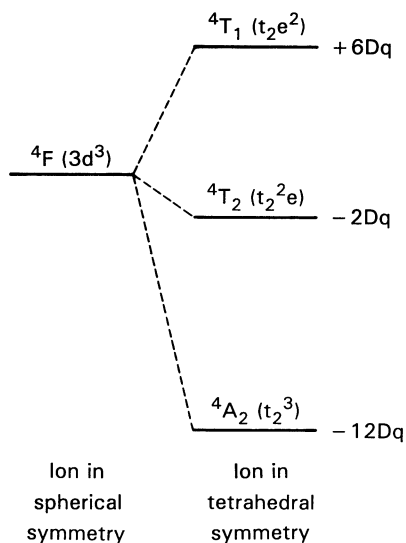


Fig. 9. Energy level scheme for the $3d^3$ configuration in tetrahedral symmetry.

with

$$P = (\mu_0/4\pi)g_e g_N \mu_B \mu_N \langle r^{-3} \rangle_{3d} \quad (14)$$

and tensor components

$$A_{ij} = \sum_{n \neq 0} \langle 0|L_i|n \rangle \langle n|L_j|0 \rangle / (E_n - E_0). \quad (15)$$

The changes of electronic and nuclear g values are thus related by

$$\Delta g_N = - (P/\lambda)(\mu_B/\mu_N) \Delta g_e. \quad (16)$$

This expression is expected still to hold in the case of equal reduction of the two shifts by covalent electron delocalisation. Therefore, using the free-ion values $P = -0.00245 \text{ cm}^{-1}$ from Morton and Preston (1978), $\lambda = 30 \text{ cm}^{-1}$ from Dunn (1961), and the observed electronic g shift $\Delta g_e = -0.0042$ from table 1, one calculates $\Delta g_N = -0.00063$. The free-ion g_N values tabulated by Fuller (1976) give $g_N = -0.31488 \pm 0.00002$ for ^{47}Ti and $g_N = -0.31496 \pm 0.00003$ for ^{49}Ti . These are the values as measured by NMR for the nuclei with diamagnetic screening by the 1s, 2s and 3s electrons. Since the screening will also be present in the solid, the uncorrected values will be used for comparison with the Si:Ti data as given in table 1. The experimental shifts Δg_N are found to be -0.00026 for the two nuclei. There is agreement in the sign and order of magnitude with the crystal field model.

Table 1
Spin Hamiltonian parameters of interstitial $^{47}\text{Ti}^+$ and $^{49}\text{Ti}^+$ in silicon.

	$^{47}\text{Ti}^+$	$^{49}\text{Ti}^+$
g_e	1.99806 ± 0.00004	1.99806 ± 0.00004
g_N	-0.31514 ± 0.00001	-0.31522 ± 0.00001
A/h (MHz)	15.64505 ± 0.00003	15.65070 ± 0.00004
U/h (kHz)	-11.05 ± 0.06	-11.10 ± 0.09
a/h (kHz)	-0.222 ± 0.005	-0.085 ± 0.005
b/h (kHz)	0.012 ± 0.001	0.005 ± 0.001

4.3. Hyperfine interaction SI

Following the perturbation calculation as referred to in the previous section, the contribution to the hyperfine interaction due to spin–orbit coupling is given by Low (1960):

$$A_{\text{so}} = P\Delta g_e. \quad (17)$$

The calculated contribution $A_{\text{so}}/h = 0.31$ MHz appears to be much smaller than the actual value. The isotropic interaction will, therefore, mainly arise from contact interaction with electrons in s orbitals. The relation between the hyperfine parameter A and the unpaired spin density $\delta\rho_{\text{Si}} \equiv |\psi_{\uparrow}(0)|^2 - |\psi_{\downarrow}(0)|^2$ is

$$A = (1/2S)^2 \mu_0 g_e g_N \mu_B \mu_N \delta\rho_{\text{Si}}. \quad (18)$$

Comparing the results for the two titanium isotopes one calculates

$$[A/g_N]^{47\text{Ti}}/[A/g_N]^{49\text{Ti}} = [\delta\rho_{\text{Si}}]^{47\text{Ti}}/[\delta\rho_{\text{Si}}]^{49\text{Ti}} = 0.99989 \pm 0.00003. \quad (19)$$

A small, but measurable, hyperfine anomaly is found. The effect is related to the different distribution of nuclear magnetic moment in the two nuclei, which is revealed by the contact electron spin density and confirms its relevance. Sources for the contact spin density are 1s and 2s electrons in valence band states, 3s electrons in valence orbitals, and electrons in 4s states. In the ENDOR experiment the sign of the hyperfine interaction was not determined. Theoretical calculations by Katayama-Yoshida and Zunger (1985) could very well reproduce the experimental value with positive sign. Accepting, therefore, $A/h = +15.65$ MHz, and using $g_N = -0.3152$, one finds with eq. (18) that $\delta\rho_{\text{Si}} = -1.26 \times 10^{30} \text{ m}^{-3}$. This result is opposite in sign to the value $\delta\rho_{4s} = +20.08 \times 10^{30} \text{ m}^{-3}$ tabulated by Morton

and Preston (1978) for an electron in a 4s orbital. Core polarisation, $\delta\rho_{cp} = -5.2 \times 10^{30} \text{ m}^{-3}$ according to Watson and Freeman (1967), is of the same sign, but considerably larger. Probably, the core polarisation forms a main contribution to the hyperfine interaction. The effect is reduced by covalent delocalisation, the required reduction factor being $\delta\rho_{Si}/\delta\rho_{cp} = 0.24$. Independent information on the delocalisation is provided by ligand ENDOR studies, as discussed in section 5. For Si:Ti⁺, considering experimental (Van Wezep et al. 1985) and theoretical (Katayama-Yoshida and Zunger 1985, Beeler et al. 1985) results, the spin density remaining on the core is estimated to be 58%, giving the reduced contribution $\delta\rho_{cp} = -3.02 \times 10^{30} \text{ m}^{-3}$. The positive deviation of the measured value by $+1.76 \times 10^{30} \text{ m}^{-3}$ can be accounted for by an admixture of 9% of a 4s orbital. This is of the same magnitude as the calculated value for the system Si:Fe_i⁰. In the analysis the polarising effect of spin in the silicon orbitals has been ignored.

4.4. Electron–nuclear interaction S^3I

The most common higher-order term, which is cubic in the electron spin S and linear in nuclear spin I , is given explicitly in its full form for cubic symmetry in the Hamiltonian equation (10). It was first observed in electron paramagnetic resonance for the Co²⁺ impurity in the semiconductors ZnTe and CdTe (Ham et al. 1960), with a coupling constant U/h of several MHz. For Ti⁺ in Si the interaction is much weaker and observable only in the ENDOR spectrum, but there it forms the main contribution to the angular dependence (fig. 8). In analogy with the treatment by Low (1960), the interaction term of type S^3I has been evaluated by several authors (Ham et al. 1960, Woodward and Chatterjee 1971, Takeuchi et al. 1979). Ham et al. (1960) considered the fourth-order perturbation contribution (Geschwind 1967)

$$U = \frac{\langle {}^4A_2 | \lambda L \cdot S | {}^4T_2 \rangle \langle {}^4T_2 | \lambda L \cdot S | {}^4T_1 \rangle \langle {}^4T_1 | PL \cdot I | {}^4T_2 \rangle \langle {}^4T_2 | \lambda L \cdot S | {}^4A_2 \rangle}{[E({}^4A_2) - E({}^4T_2)]^2 [E({}^4A_2) - E({}^4T_1)]}. \quad (20)$$

Upon evaluation of the matrix elements this yields

$$U = 120P\lambda^3/[E({}^4A_2) - E({}^4T_2)]^2 [E({}^4A_2) - E({}^4T_1)]. \quad (21)$$

Using the crystal field results $[E({}^4A_2) - E({}^4T_2)]/[E({}^4A_2) - E({}^4T_1)] = \frac{5}{9}$ and electron g shift $\Delta g_e = -8\lambda/[E({}^4T_2) - E({}^4A_2)]$ this was re-expressed as

$$U = -(25/192)P\Delta g_e^3. \quad (22)$$

Substituting the experimentally observed g shift and the free-ion value for P , one obtains $U/h = -7 \times 10^{-4} \text{ kHz}$, which is several orders of magnitude less

than the actual value (table 1). Several improvements on the scheme of calculation have been investigated (Woodward and Chatterjee 1971, Takeuchi et al. 1979), such as the inclusion of spin–spin and other interactions and states from terms other than 4F . In none of the cases a satisfactory agreement was obtained. Among the handicaps met are the insufficient knowledge of the energy positions of the states and of the degree of covalency between the impurity and the semiconductor crystal.

4.5. Electron–nuclear interaction S^2I^2

If in a perturbation calculation analogous to eq. (20) the interactions $PL \cdot I$ and $\lambda L \cdot S$ are taken twice, a term of type S^2I^2 is generated (Geschwind 1967). These terms are magnetic in origin, but as they transform in the same way as the real electric–nuclear quadrupole interaction, they are often referred to as pseudo-quadrupolar interactions. One expects such terms to be smaller than the S^3I terms by roughly the factor $P/\lambda \cong 10^{-4}$. With $U/h \cong -11$ kHz the expected coefficients for the S^2I^2 terms are, thus, $\cong 1$ Hz, much less than the actually found values, and also very much less than the ENDOR linewidth. The true electric–nuclear quadrupole interaction may be present even for an S-state ion in cubic symmetry. As evidenced by the g shift, some orbital angular momentum has been mixed into the ground state. This will create the electric field gradient coupling with the nuclear quadrupole moment. In cubic symmetry the interaction is described by two spin operators with independent constants as given in eq. (10) (Geschwind 1967, Bleaney 1967). Bleaney (1967) has given explicit expressions for the coefficients:

$$a = -\frac{3}{4}ne^2Q\langle r^{-3} \rangle/I(2I-1), \quad (23a)$$

$$b = -\frac{1}{6}me^2Q\langle r^{-3} \rangle/I(2I-1). \quad (23b)$$

As expected, the expressions show the proportionality of the interaction with the nuclear electric quadrupole moment Q . Applying this to the comparison of the two Ti isotopes, one obtains

$$a({}^{49}\text{Ti})/a({}^{47}\text{Ti}) = b({}^{49}\text{Ti})/b({}^{47}\text{Ti}) = 10Q({}^{49}\text{Ti})/21Q({}^{47}\text{Ti}). \quad (24)$$

Using the tabulated values for the nuclear quadrupole moments from Fuller (1976), $Q({}^{49}\text{Ti}) = 0.24 \times 10^{-28} \text{ m}^2$ and $Q({}^{47}\text{Ti}) = 0.29 \times 10^{-28} \text{ m}^2$, the ratio of coefficients in eq. (24) should be 0.39 ± 0.02 . Experimentally, the data in table 1 give 0.38 ± 0.02 for a and 0.42 ± 0.11 for b . It is, therefore, concluded that the S^2I^2 term is caused by an interaction which involves the nuclear electric quadrupole moment linearly. From $a/b \cong -20$ the ratio n/m , which equals 1 in spherical symmetry, is found to be $\cong -4$ in cubic symmetry.

5. Ligand-atom ENDOR

5.1. Ligand-atom shells

Hyperfine interactions with ligand atoms in a silicon crystal can be experienced by virtue of the presence of ^{29}Si nuclei with nuclear spin $I = \frac{1}{2}$. Each lattice site has the 4.7% probability of its natural abundance to be occupied by such an isotope. By applying the symmetry operations of the group 43m to a lattice site on a general position with respect to the impurity site, a shell of 24 symmetry-related sites is generated. For nuclei in one shell also the ENDOR frequencies are related. On rotation of the magnetic field, e.g. in a $(0\bar{1}1)$ plane, characteristic patterns are generated showing the orientational degeneracy. For a nucleus on a general site the symmetry of the electron-nuclear system formed by the paramagnetic impurity plus the nuclear magnetic ^{29}Si isotope is only of point group 1. An experimental pattern, again taken from ENDOR studies of $\text{Si}:\text{Ti}^+$ (Van Wezep et al. 1985), is shown in fig. 10a. If the initial site is chosen on a $\{011\}$ mirror plane through the impurity ion, the symmetry will still be m and a shell will contain 12 lattice sites. Atoms labelled 3 in fig. 11 form part of a shell of this type. The number of ENDOR lines is reduced and the pattern generated for the usual variation of B in the $(0\bar{1}1)$ plane is given in fig. 10b. Starting from a position on a $\langle 100 \rangle$ axis through the central ion, symmetry 2mm, a shell with six sites is generated. Atoms labelled 2 in fig. 11 are examples of one such shell. The ENDOR frequencies for all atoms in the shell together form the pattern as given in fig. 10c. Finally, for atoms on a $\langle 111 \rangle$ axis through the impurity, with remaining symmetry 3m for the system, a shell contains four symmetry-related sites. Atoms labelled 1, 4 and 5 in fig. 11 are three examples of such shells close to the impurity. The pattern for rotation of B is given in fig. 10d. The angular dependence revealed by the patterns allows the allocation of magnetic nuclei to lattice sites of the associated symmetry.

5.2. LCAO analysis

Further discussions of ligand ENDOR will again be illustrated by the results obtained for interstitial titanium in silicon. Hyperfine tensors describing the interactions with nuclei in four shells of type 1, eight shells of type m, one shell of type 2mm and four shells of type 3m were reported (Van Wezep et al. 1985). The 214 lattice sites in these 17 shells provide a detailed mapping of the spin density around the impurity. For quantitative analysis the wave functions for the paramagnetic electrons are approximated by the linear combination of atomic orbitals method. In analogy with the classification of

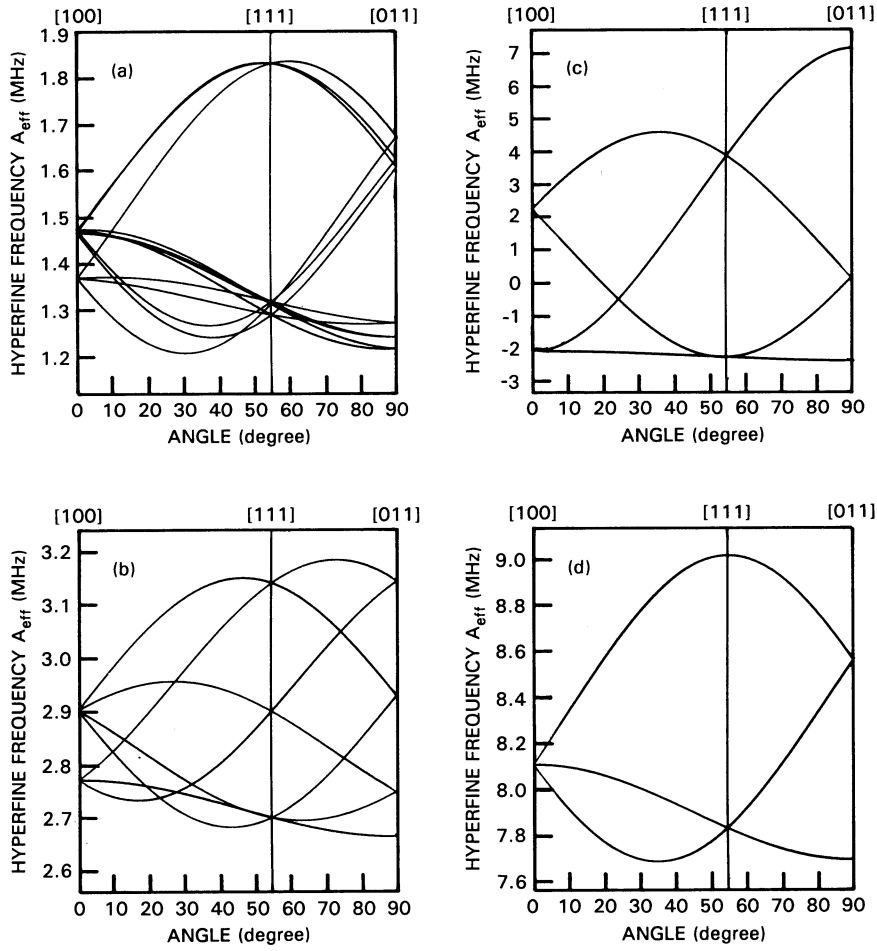


Fig. 10. Angular dependence of the effective hyperfine interaction A_{eff} for the four symmetry types of shells on rotation of the magnetic field in the (011) plane: (a) shell class 1; (b) shell class m; (c) shell class 2mm; (d) shell class 3m.

atoms in shells, symmetrised shell orbitals are constructed. For Si:Ti^+ the three electrons in the $3d^3$ configuration are in states transforming as the t_2 -irreducible representation of the $\bar{4}3m$ point group. The ligand orbitals are symmetrised accordingly. Schematically, this gives the one-electron orbitals

$$\psi_{xy} = \alpha d_{xy} + \sum_i \psi_{xy, 1, i} + \sum_i \psi_{xy, m, i} + \sum_i \psi_{xy, 2mm, i} + \sum_i \psi_{xy, 3m, i}, \quad (25a)$$

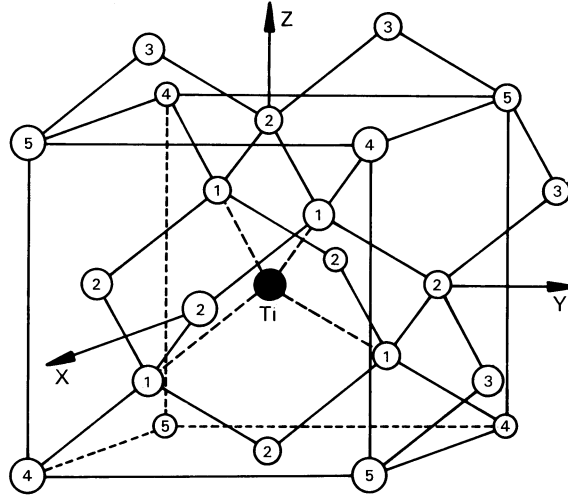


Fig. 11. The interstitial titanium atom (solid black sphere) surrounded by silicon atoms, for which the shell structure is indicated.

$$\psi_{yz} = \alpha d_{yz} + \sum_i \psi_{yz,1,i} + \sum_i \psi_{yz,m,i} + \sum_i \psi_{yz,2mm,i} + \sum_i \psi_{yz,3m,i}, \quad (25b)$$

$$\psi_{zx} = \alpha d_{zx} + \sum_i \psi_{zx,1,i} + \sum_i \psi_{zx,m,i} + \sum_i \psi_{zx,2mm,i} + \sum_i \psi_{zx,3m,i}, \quad (25c)$$

where the index i enumerates the summation over shells. In a more explicit form the three shell orbitals for the case of $\langle 111 \rangle$ site atoms, symmetry $3m$, are given as

$$\begin{aligned} \psi_{xy,3m,i} = & + \frac{1}{2} \beta_i (s_1 - s_2 - s_3 + s_4) + \frac{1}{2} \gamma_i (\sigma_1 - \sigma_2 - \sigma_3 + \sigma_4) \\ & + \frac{1}{4} \delta_i [(-\pi_{1x} + \pi_{2x} + \pi_{3x} - \pi_{4x}) \\ & + \sqrt{3}(\pi_{1y} - \pi_{2y} - \pi_{3y} + \pi_{4y})], \end{aligned} \quad (26a)$$

$$\begin{aligned} \psi_{yz,3m,i} = & + \frac{1}{2} \beta_i (s_1 - s_2 + s_3 - s_4) + \frac{1}{2} \gamma_i (\sigma_1 - \sigma_2 + \sigma_3 - \sigma_4) \\ & + \frac{1}{4} \delta_i [(-\pi_{1x} + \pi_{2x} - \pi_{3x} + \pi_{4x}) \\ & - \sqrt{3}(\pi_{1y} - \pi_{2y} + \pi_{3y} - \pi_{4y})], \end{aligned} \quad (26b)$$

$$\begin{aligned} \psi_{zx,3m,i} = & + \frac{1}{2} \beta_i (s_1 + s_2 - s_3 - s_4) + \frac{1}{2} \gamma_i (\sigma_1 + \sigma_2 - \sigma_3 - \sigma_4) \\ & + \frac{1}{2} \delta_i (\pi_{1x} + \pi_{2x} - \pi_{3x} - \pi_{4x}). \end{aligned} \quad (26c)$$

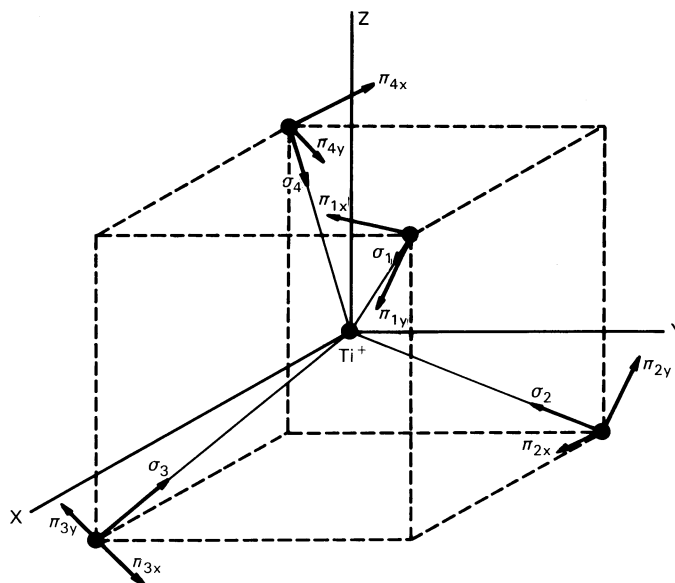


Fig. 12. Orientations of σ and π orbitals on the four atoms of a shell type $3m$.

The indices 1, 2, 3 and 4 refer to the ligands at positions nnn , $\bar{n}n\bar{n}$, $n\bar{n}\bar{n}$ and $\bar{n}\bar{n}n$, respectively. Figure 12 also illustrates the σ orbitals pointing from the ligand to the centre, and the perpendicular π orbitals which for site 1 point along $[1\bar{2}1]$ and $[10\bar{1}]$. Parameters β_i , γ_i and δ_i are the expansion coefficients to be determined in the analysis. Similar expressions hold for shells of other symmetry. In deriving the matrix elements for the hyperfine interaction, contributions from electron spin density on sites other than the one considered here are neglected, with the exception of the contribution from the central titanium ion, which is calculated in the point dipole approximation. For site 1 in a $3m$ shell the relevant part of the ligand wave function then is

$$\psi_{xy, 3m, i} = +\frac{1}{2}\beta_i s_1 + \frac{1}{2}\gamma_i \sigma_1 + \frac{1}{4}\delta_i (-\pi_{1x} + \sqrt{3}\pi_{1y}), \quad (27a)$$

$$\psi_{yz, 3m, i} = +\frac{1}{2}\beta_i s_1 + \frac{1}{2}\gamma_i \sigma_1 + \frac{1}{4}\delta_i (-\pi_{1x} - \sqrt{3}\pi_{1y}), \quad (27b)$$

$$\psi_{zx, 3m, i} = +\frac{1}{2}\beta_i s_1 + \frac{1}{2}\gamma_i \sigma_1 + \frac{1}{2}\delta_i \pi_{1x}. \quad (27c)$$

Summing over the three electrons one obtains for the isotropic part of the hyperfine tensor,

$$a = (1/2S)^{\frac{3}{4}} \beta_i^2 a_0, \quad (28)$$

with

$$a_0 = \frac{2}{3} \mu_0 g_e \mu_B g_N \mu_N |s_1(0)|^2. \quad (29)$$

On its own principal axes, $z \parallel [111]$, the anisotropic part of the tensor is given by its principal values

$$B_{xx} = B_{yy} = -(1/2S) \left(\frac{3}{4} \gamma_i^2 - \frac{3}{8} \delta_i^2 \right) b_0 - (1/2S) 3\alpha^2 b_{dd}, \quad (30a)$$

$$B_{zz} = -2B_{xx}, \quad (30b)$$

with

$$b_0 = \frac{2}{3} (\mu_0/4\pi) g_e \mu_B g_N \mu_N \langle r^{-3} \rangle_p \quad (31)$$

and

$$b_{dd} = (\mu_0/4\pi) g_e \mu_B g_N \mu_N R^{-3}. \quad (32)$$

R is the distance between the ligand site and the titanium atom.

5.3. Minimum-transferred spin density

Equations (28) and (29) directly allow the calculation of the s-type spin density. For a_0 one calculates, with $|s_1(0)|^2 = 3.451776 \times 10^{31} \text{ m}^{-3}$ from Morton and Preston (1978), $g_e = 1.99806$ (Van Wezep and Ammerlaan 1985) and $g_N = -1.1097$ (Sprenger et al. 1987), $a_0/h = -4536 \text{ MHz}$. With $S = \frac{3}{2}$

$$\beta_i^2 = 4(a/h)/(a_0/h). \quad (33)$$

In order of this analysis to be physically meaningful the sign of a , which is not determined in the experiment, must be taken as negative. Experimental ENDOR data for four type-3m shells of Si:Ti⁺ together with the results of analysis are given in table 2.

Evaluation of the anisotropic tensor is less straightforward. Equations (30a) and (30b) indicate that γ_i^2 and δ_i^2 cannot be determined separately from

Table 2

Parameters of hyperfine interactions and LCAO analysis for type-3m shells of Si:Ti⁺. Coefficient $\frac{3}{4}\gamma_i^2 - \frac{3}{8}\delta_i^2$ is calculated for $\alpha = 0$.

Shell no.	A_{\parallel}/h (MHz)	A_{\perp}/h (MHz)	a/h (MHz)	B_{zz}/h (MHz)	β^2	$\frac{3}{4}\gamma_i^2 - \frac{3}{8}\delta_i^2$	γ_i^2	δ_i^2
1	-9.0069	-7.6820	-8.1236	-0.8833	0.0071	+0.0116	0.0155	0
2	-0.0605	-2.0951	-1.4169	+1.3564	0.0012	-0.0179	0	0.0477
3	-0.7715	-0.7370	-0.7485	-0.0230	0.0007	+0.0003	0.0004	0
4	-0.0931	-0.1476	-0.1294	+0.0363	0.0001	-0.0005	0	0.0013

the experimental result: only $\gamma_i^2 - \frac{1}{2}\delta_i^2$ can be calculated. Hence, the transferred spin density $\beta_i^2 + \gamma_i^2 + \delta_i^2$ cannot be obtained from the hyperfine data. The opposite contributions to the hyperfine tensor from σ and π orbitals tend to hide the interaction. In case $\delta_i^2 = 2\gamma_i^2$, no anisotropic ligand hyperfine interaction is observed, while spin can be still present in the σ and π orbitals. As a consequence, the transferred spin density may be underestimated. Nevertheless, a minimum amount of spin transferred can be derived by putting, depending upon the sign of B_{zz} , either γ_i^2 or δ_i^2 equal to zero. This procedure was followed to determine the so-called minimum-transferred spin density (MTSD). Experimental data for the 3m shells are given in table 2. The different signs for B_{zz} indicate the alternating predominance of σ and π orbital contributions. For spin density $\alpha^2 = 0$ on the central site the minimum p (σ or π) orbital coefficient is given in the table. For conversion $b_0/h = -113.855679$ MHz was used, based on $\langle r^{-3} \rangle_p = 1.815978 \times 10^{31} \text{ m}^{-3}$ from Morton and Preston (1978). For varying values of α^2 the results are plotted in fig. 13a. For the shells of the 1, m and 2mm symmetry the analysis was also carried out and led to a similar determination of the MTSD. The total over all the shells as a function of α^2 is presented in fig. 13b. The dashed line $1 - \alpha^2$ represents the normalisation condition. In order not to violate normalisation,

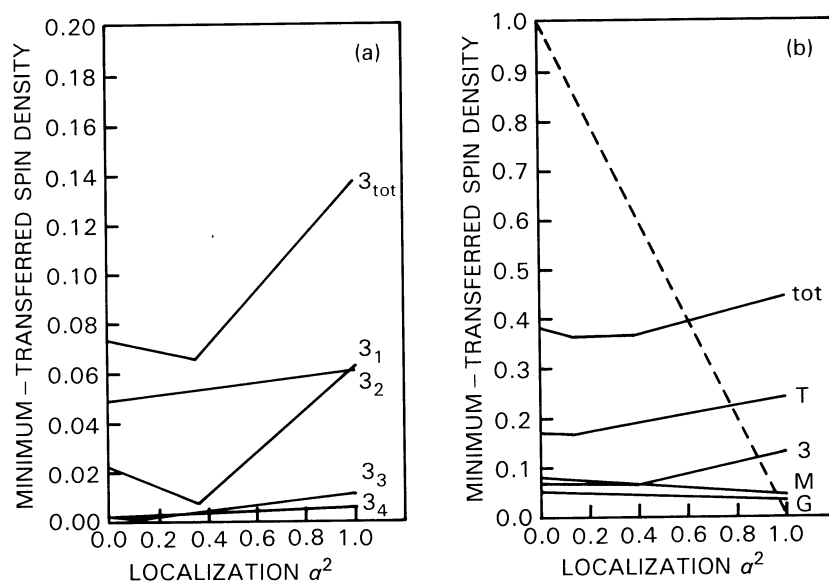


Fig. 13. Minimum of spin densities transferred to the lattice atoms (MTSD) as a function of the localisation α^2 on the Ti^+ atom for (a) the atoms in four shells of type 3m and (b) the total over ligand atoms in all shells. The dashed line $1 - \alpha^2$ represents the delocalised spin density.

α^2 must be less than 0.62. Thus, the amount of spin transferred covalently to the silicon crystal is at least 38%.

References

- Beeler, F., O.K. Andersen and M. Scheffler, 1985, *Phys. Rev. Lett.* **55**, 1498.
 Biehl, R., M. Plato and K. Möbius, 1975, *J. Chem. Phys.* **63**, 3515.
 Bleaney, B., 1967, in: *Hyperfine Interact.*, eds A.J. Freeman and R.B. Frankel (Academic Press, New York) p. 1.
 Dunn, T.M., 1961, *Trans. Faraday Soc.* **57**, 1441.
 DuVarney, R.C., J.R. Niklas and J.-M. Spaeth, 1981, *Phys. Status Solidi b* **103**, 329.
 Feher, G., 1956a, *Phys. Rev.* **103**, 500.
 Feher, G., 1956b, *Phys. Rev.* **103**, 834.
 Feher, G., 1957, *Phys. Rev.* **105**, 1122.
 Feher, G., 1959, *Phys. Rev.* **114**, 1219.
 Feher, G., and E.A. Gere, 1956, *Phys. Rev.* **103**, 501.
 Feher, G., C.S. Fuller and E.A. Gere, 1957, *Phys. Rev.* **107**, 1462.
 Fuller, G.H., 1976, *J. Phys. Chem. Ref. Data* **5**, 835.
 Geschwind, S., 1967, in: *Hyperfine Interact.*, eds A.J. Freeman and R.B. Frankel (Academic Press, New York) p. 225.
 Greulich-Weber, S., 1987, Ph.D. Thesis, University of Paderborn.
 Hage, J., J.R. Niklas and J.-M. Spaeth, 1986, *Mater. Sci. Forum* **10-12**, 259.
 Hale, E.B., and R.L. Mieher, 1969, *Phys. Rev.* **184**, 739.
 Ham, F.S., G.W. Ludwig, G.D. Watkins and H.H. Woodbury, 1960, *Phys. Rev. Lett.* **5**, 468.
 Katayama-Yoshida, H., and A. Zunger, 1985, *Phys. Rev. B* **31**, 8317.
 Low, W., 1960, *Solid State Phys.*, Suppl. 2, eds F. Seitz and D. Turnbull (Academic Press, New York).
 Morton, J.R., and K.F. Preston, 1978, *J. Magn. Res.* **30**, 577.
 Niklas, J.R., and J.-M. Spaeth, 1980, *Phys. Status Solidi b* **101**, 221.
 Niklas, J.R., R.U. Bauer and J.-M. Spaeth, 1983, *Phys. Status Solidi b* **119**, 171.
 Spaeth, J.-M., and J.R. Niklas, 1981, *Recent Developments in Condensed Matter Physics* **1**, 393.
 Sprenger, M., S.H. Muller, E.G. Sieverts and C.A.J. Ammerlaan, 1987, *Phys. Rev. B* **35**, 1566.
 Takeuchi, H., K. Horai and M. Arakawa, 1979, *J. Phys. Soc. Jpn.* **46**, 18.
 Ueda, Y., J.R. Niklas, J.-M. Spaeth, U. Kaufmann and J. Schneider, 1983, *Solid State Commun.* **46**, 127.
 Van Wezep, D.A., and C.A.J. Ammerlaan, 1985, *J. Electron. Mater.* **14A**, 863.
 Van Wezep, D.A., and C.A.J. Ammerlaan, 1988, *Phys. Rev. B* **37**, 7268.
 Van Wezep, D.A., R. van Kemp, E.G. Sieverts and C.A.J. Ammerlaan, 1985, *Phys. Rev. B* **32**, 7129.
 Watson, R.E., and A.J. Freeman, 1967, in: *Hyperfine Interact.*, eds A.J. Freeman and R.B. Frankel (Academic Press, New York) p. 53.
 Woodward, A.S., and R. Chatterjee, 1971, *J. Phys. C* **4**, 1378.